Fieldlike spin-orbit torque in ultrathin polycrystalline FeMn films

Yumeng Yang,[1,2] Yanjun Xu,[1] Xiaoshan Zhang,[1] Ying Wang,[1] Shufeng Zhang,[3] Run-Wei Li,[4] Meysam Sharifzadeh Mirshekarloo,[2] Kui Yao,[2] and Yihong Wu[1,*]

[1]*Department of Electrical and Computer Engineering, National University of Singapore, 4 Engineering Drive 3, Singapore 117583, Singapore*

[2]*Institute of Materials Research and Engineering (IMRE), Agency for Science, Technology and Research (A*STAR), 08-03, 2 Fusionopolis Way, Innovis, 138634, Singapore*

[3]*Department of Physics, University of Arizona, Tucson, Arizona 85721, USA*

[4]*Key Laboratory of Magnetic Materials and Devices, Ningbo Institute of Materials Technology and Engineering, Chinese Academy of Sciences, Ningbo 315201, People's Republic of China*

(Received 18 October 2015; revised manuscript received 1 February 2016; published 3 March 2016)

Fieldlike spin-orbit torque in FeMn/Pt bilayers with ultrathin polycrystalline FeMn has been characterized through planar Hall effect measurements. A large effective field of 2.05×10^{-5} to 2.44×10^{-5} Oe (A^{-1} cm^2) is obtained for FeMn in the thickness range of 2–5 nm. The experimental observations can be reasonably accounted for by using a macrospin model under the assumption that the FeMn layer is composed of two spin sublattices with unequal magnetizations. The large effective field corroborates the spin Hall origin of the effective field, considering the much smaller uncompensated net moments in FeMn as compared to NiFe. The effective absorption of spin current by FeMn is further confirmed by the fact that spin current generated by Pt in NiFe/FeMn/Pt trilayers can only travel through the FeMn layer with a thickness of 1–4 nm. By quantifying the fieldlike effective field induced in NiFe, a spin diffusion length of 2 nm is estimated in FeMn, consistent with values reported in the literature by ferromagnetic resonance and spin-pumping experiments.

DOI: 10.1103/PhysRevB.93.094402

I. INTRODUCTION

Spin-orbit torque (SOT) effect, arising from nonequilibrium spin density induced by either local or nonlocal strong spin-orbit (SO) interaction, has been demonstrated as a promising technique to control magnetization of ferromagnets (FMs) [1–5]. Although the SO coupling-induced spin polarization of electrons has been studied extensively in semiconductors, the investigations of SO-induced nonequilibrium spin density in FMs and the resultant SOT on local magnetization have only been reported recently. Manchon and Zhang [6] predicted theoretically that, in the presence of a Rashba SO coupling, the SOT is able to switch the magnetization of a single magnetic two-dimensional electron gas at a current density of about $10^4 - 10^6$ A cm^{-2}. This value is lower than or comparable to the critical current density of typical spin-transfer torque (STT) devices. To our knowledge, the first experimental observation of SOT was reported by Chernyshov *et al.* [1] for a $Ga_{0.94}Mn_{0.06}As$ dilute magnetic semiconductor (DMS) with a Curie temperature of 80 K. The $Ga_{1-x}Mn_xAs$ layer grown epitaxially on GaAs (001) substrate is compressively strained, which results in a Dresselhaus-type SO interaction that is linear in momentum. When a charge current passes through the DMS layer below its Curie temperature, the resultant SOT was able to switch the magnetization with the assistance of an external field and crystalline anisotropy. The lack of bulk inversion asymmetry (BIA) in transition metal FM has prompted researchers to explore the SOT effect in FM heterostructures with structure inversion asymmetry (SIA). Miron *et al.* [2] reported the first observation, as far as we know, of a current-induced SOT in a thin Co layer sandwiched by a Pt and an AlO_x layer. Due to the asymmetric interfaces with Pt and AlO_x, electrons in the Co layer experience a large Rashba effect, leading to sizable current-induced SOT. The Pt layer is crucial because, otherwise, the Rashba effect due to SIA alone would be too weak to cause any observable effect in the Co layer. At the same time, the presence of Pt also gives rise to a complex scenario about SOT in FM/heavy metal (HM) bilayers. In this case, in addition to the Rashba SOT, spin current diffused from the Pt layer due to spin Hall effect (SHE) also exerts a torque on the FM layer through transferring the spin angular momentum to the local magnetization [4]. To differentiate it from the Rashba SOT, it is also called SHE-SOT. Although the exact mechanism still remains debatable, both types of torques are generally present in the FM/HM bilayers. The former is fieldlike, while the latter is of antidamping nature similar to STT. Mathematically, the two types of torques can be modeled by $\vec{T}_{\mathrm{FL}} = \tau_{\mathrm{FL}}\vec{m} \times (\vec{j} \times \vec{n})$ (fieldlike) and $\vec{T}_{\mathrm{DL}} = \tau_{\mathrm{DL}}\vec{m} \times [\vec{m} \times (\vec{j} \times \vec{n})]$ (antidampinglike), respectively, where $\vec{m}$ is the magnetization direction, $\vec{j}$ is the in-plane current density, $\vec{n}$ is the interface normal, and τ_{FL} and τ_{DL} are the magnitudes of the fieldlike and antidampinglike torques [7–9]. Following the first report of Miron *et al.* [2], the SOT has been reported in several FM/HM bilayers with FMs such as CoFeB [5,7–10], Fe [11], NiFe [12], etc., and HMs such as Pt and Ta. An average effective field strength of around 4×10^{-6} Oe (A^{-1} cm^2) has been obtained, except for the Pd/Co multilayer system [13], which was reported to have a very large H_{eff}/j value in the range of 10^{-5} Oe (A^{-1} cm^2). A higher effective field-to-current ratio is desirable for device applications because it will lead to a smaller critical current that is required for magnetization reversal. The critical current density for Rashba-type SOT is given by [6] $j_{\mathrm{critical}} = \frac{\hbar e H_A M_s}{2\alpha_R m P}$, where H_A is the uniaxial anisotropy field, M_s the saturation

*elewuyh@nus.edu.sg

magnetization, α_R the Rashba constant, P the electron spin polarization, m the electron mass, e the electron charge, and $\hbar$ the Planck constant. On the other hand, the antidampinglike effective field H_{DL} induced by the adjacent HM layer to current density ratio can be expressed as [4] $H_{\mathrm{DL}}/j_c = \frac{\hbar}{2e}\frac{\theta_{\mathrm{SH}}}{M_s t_{\mathrm{FM}}}$ where θ_{SH} is the spin Hall angle of HM, t_{FM} the thickness of FMs, and j_c the charge current. More recent studies [14,15] suggest that the spin Hall originated fieldlike effective field in FM/HM bilayers can also be parameterized using the same equation by replacing θ_{SH} with an effective spin Hall angle θ_{FL}, i.e., $H_{\mathrm{FL}}/j_c = \frac{\hbar}{2e}\frac{\theta_{\mathrm{FL}}}{M_s t_{\mathrm{FM}}}$. Regardless of the role of the two types of SOT, these results suggest that FMs with low M_s are desirable for investigating and exploiting the SOT effect. Of our particular interest are anti-FMs (AFMs) with small net moments due to uncompensated spins, which can potentially lead to large SOT effect in AFM/HM bilayers. In addition, AFMs are also promising for future spintronics applications due to their negligible stray field, large anisotropy, and fast spin dynamics, all of which can potentially lead to AFM-based spintronic devices with improved downscaling capability, thermal stability, and speed, as compared to their FM counterparts [16,17].

Unlike FM, studies on the interactions between nonequilibrium spins or spin current with AFM are quite limited. It has been predicted theoretically that STT can act on AFM, causing reorientation of its spin configuration, domain wall motion, and stable oscillation or precession of the Neel vector [18–21]. Several follow-up experiments on exchange-biased spin valves [22–25] have shown that current-induced STT is able to affect the exchange bias at the FM/AFM interface, indirectly suggesting the presence of STT effect in AFM. More recently, spin pumping and spin torque ferromagnetic resonance (ST-FMR) measurements on FM/AFM/HM trilayers demonstrated that spin current can travel across both NiO and IrMn at a reasonably large distance and high efficiency [26–30]. Although spin fluctuation is believed to play an important role in the spin current transport in the AFM, the real mechanism remains not well understood at present. In addition to NiO and IrMn, which have been shown to be efficient "channels" for spin-current transport, it would be of equal interest to know if there is any AFM which shows just the opposite behavior, i.e., functioning as an efficient absorber for the spin current, and if so, whether the absorbed spin current can exert a torque on the magnetization of the AFM. If such an AFM or phenomenon indeed exists, can we quantify the torque or effective field generated in the AFM experimentally? The answer to these questions will help to determine the potential role of AFMs in future spintronic devices other than their existing role as merely a pinning layer for FMs. In this regard, in this paper, we investigate the spin-current-induced effects in FeMn/Pt bilayers. We choose to focus on FeMn because it is the "softest" among the Mn-based AFMs that have been studied for exchange bias applications; therefore, in case there is any SOT effect in the bilayers, it can be detected easily through planar Hall effect (PHE) measurement. Recent studies have also shown that the spin Hall angle of FeMn is the smallest among PtMn, IrMn, PdMn, and FeMn [31,32]. This will facilitate the study of spin-current transport across the FeMn/Pt interface because the role of FeMn as a spin-current generator can be neglected.

In order to investigate the SOT effect in FeMn/Pt bilayers, we fabricated a series of FeMn/Pt bilayers with different FeMn thicknesses and then characterized them through PHE measurements. Clear FM-like PHE signals were observed in FeMn/Pt bilayers with the FeMn thicknesses ranging from 2 to 5 nm. Magnetometry measurements of coupon films suggest that the FM-like behavior originates from canting of spin sublattices in the FeMn layer. Using the second-order PHE measurement method [10,12], a fieldlike effective field-to-current ratio in the range of 2.05×10^{-5} to 2.44×10^{-5} Oe ($\mathrm{A}^{-1}\,\mathrm{cm}^2$) was extracted, which is nearly two orders of magnitude larger than the typical value of 4.01×10^{-7} Oe ($\mathrm{A}^{-1}\,\mathrm{cm}^2$) for NiFe/Pt bilayers. The significantly large effective field value is understood as a result of much smaller net moments from canting of the uncompensated spins in the AFM as compared to its FM counterpart. Further investigations on NiFe/FeMn/Pt trilayers using the same PHE measurements confirm that the spin current generated by Pt is largely absorbed by FeMn, and it can only travel through FeMn with a thickness of 1–4 nm. A spin-diffusion length of around 2 nm in FeMn is obtained by quantifying the fieldlike effective field induced in NiFe, which is comparable to the ST-FMR [33] and spin-pumping [32] measurements. Our results suggest that, in ultrathin polycrystalline AFMs, due to the relatively small exchange field between spin sublattices, the spin current can interact with AFMs, causing reorientation of the spin sublattices, in a similar way as it does with the FMs.

The remainder of this paper is organized as follows. Section II describes the experimental details. Section III A presents the structural and magnetic properties of the as-deposited FeMn film. Section III B discusses the magnetoresistance (MR) of NiFe/FeMn/Pt trilayer Hall bars. In Secs. III C and III D, we present and discuss the electrical measurement results of FeMn/Pt bilayers. The electrical measurement results of NiFe/FeMn/Pt trilayers are presented and discussed in Sec. III E, followed by conclusions in Sec. IV.

II. EXPERIMENTAL DETAILS

As illustrated in Fig. 1(a), two series of samples in the form of Hall bars [Fig. 1(b)] were prepared on SiO_2(300 nm)/Si substrates with the following configurations: (i) Si/SiO_2/FeMn(t_{FeMn})/Pt(3) and (ii) Si/SiO_2/Ta(3)/NiFe(3)/FeMn(t_{FeMn})/Pt(3) (number in the parentheses indicates the thickness in nanometers). The thickness (t_{FeMn}) of FeMn was varied in the range of 0–15 nm to investigate its effect on transport properties. Throughout this paper, we adopt the convention that multilayers always start from the substrate side, e.g., FeMn/Pt refers to Si/SiO_2/FeMn/Pt. The Hall bars, with a central area of 2.3×0.2 mm and transverse electrodes of 0.1×1 mm, were fabricated using combined techniques of photolithography and sputtering deposition. The former was performed using a Microtech LaserWriter, and the latter was carried out using a dc magnetron sputter with a base and process pressure of 3×10^{-8} Torr and 3 mTorr, respectively. During the deposition of the trilayers, an in-plane bias field of ~500 Oe was applied along the long axis of the Hall bar to induce an in-plane easy axis in NiFe. The resistivity of individual layers was extracted from the overall resistivity of bilayers with thicknesses in the same range as those

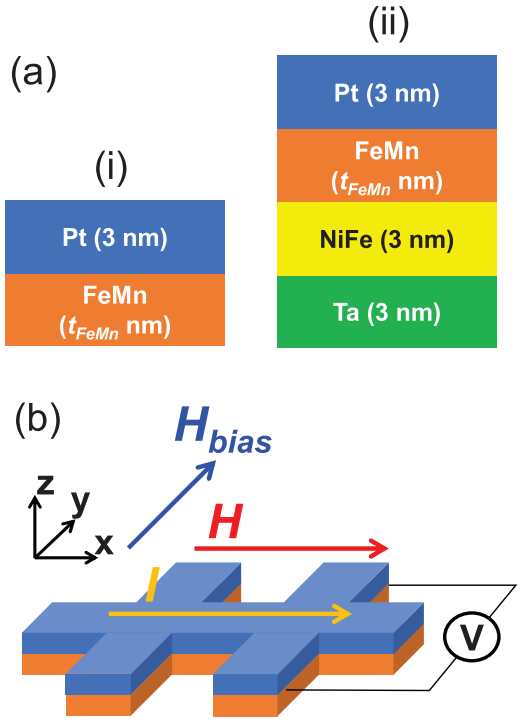

FIG. 1. (a) Schematic of (i) FeMn/Pt bilayer and (ii) NiFe/FeMn/Pt trilayers samples. (b) Schematic of the second-order PHE measurement setup with a transverse bias field ($H_{\rm bias}$).

for transport measurements but with different thickness combinations, and the obtained resistivity values are: $\rho_{\rm Ta} = 159\,\mu\Omega\cdot$cm, $\rho_{\rm NiFe} = 79\,\mu\Omega\cdot$cm, $\rho_{\rm FeMn} = 166\,\mu\Omega\cdot$cm, and $\rho_{\rm Pt} = 32\,\mu\Omega\cdot$cm.

All electrical measurements were carried out at room temperature (RT) using the Keithley 6221 current source and 2182A nanovolt meter. The PHE measurements were performed by supplying a dc bias current (I) to the Hall bar and measuring the Hall voltage (V_{xy}) while sweeping an external field (H) in x-axis direction [see schematic in Fig. 1(b)]. Second-order PHE measurements were carried out to quantify the spin-current-induced effective field in both FeMn/Pt bilayers and NiFe/FeMn/Pt trilayers [10,12]. In this method, a set of second-order PHE voltages, defined as $\Delta V_{xy}(H_{\rm bias}) = V_{xy}(+I, +H_{\rm bias}, H) + V_{xy}(-I, -H_{\rm bias}, H)$, are obtained from the algebraic sum of the first-order Hall voltages measured at a positive ($+I$) and negative bias ($-I$) current, respectively, at three different transverse bias fields in the y-axis direction: $-H_{\rm bias}$, 0 and $H_{\rm bias}$. Here, I is the current applied, H is the external field in x-axis direction, and V_{xy} is the first-order Hall voltage. Under the small perturbation assumption, i.e., both the current-induced field ($H_{\rm FL}$) and applied transverse bias field ($H_{\rm bias}$) are much smaller than the external field (H), the change in in-plane magnetization direction is proportional to $(H_I + H_{\rm bias})/H_{\rm eff}$, where H_I is the sum of $H_{\rm FL}$ and Oersted field ($H_{\rm Oe}$), and $H_{\rm eff}$ is the sum of H and anisotropy field (H_A). The linear dependence of second-order PHE voltage on the algebraic sum of H_I and $H_{\rm bias}$ allows one to determine the effective field by varying $H_{\rm bias}$ as both fields play an equivalent role in determining the magnetization direction. After some algebra, it is derived that $\frac{\Delta V_{xy}(0)}{\Delta V_{xy}(H_{\rm bias})-\Delta V_{xy}(-H_{\rm bias})} = \frac{H_{\rm FL}+H_{\rm Oe}}{2H_{\rm bias}}$. By linearly fitting $\Delta V_{xy}(0)$ against $[\Delta V_{xy}(H_{\rm bias}) - \Delta V_{xy}(-H_{\rm bias})]$, the ratio of $(H_{\rm FL} + H_{\rm Oe})$ to $2H_{\rm bias}$ can be determined from the slope of the curve. After subtraction of $H_{\rm Oe}$ from H_I, the current induced $H_{\rm FL}$ at a specific bias current can thus be obtained. Although the second-order PHE method was initially developed for quantifying the effective field in NiFe/Pt bilayers, as we will discuss later, it can also be applied to FeMn/Pt bilayers by dividing the FeMn into two spin sublattices with unequal magnetizations. The same procedure can also be used to determine the effective field in NiFe in NiFe/FeMn/Pt trilayers as, in this case, the PHE signal is mainly from the NiFe layer, and the signal from FeMn can be neglected.

To further confirm the SOT effect in FeMn/Pt bilayers, spin Hall MR (SMR) measurements were performed on these bilayers with different FeMn thicknesses. It has been reported in the FM/HM cases [34,35], SMR has the same origin with the antidampinglike effective field $H_{\rm DL}$. As shown in the schematic of Fig. 2(a), when a charge current j_c flows in the x direction, a spin current j_s is generated from the Pt layer through SHE. The spin current follows in the z direction with the spin polarization $\vec{\sigma}$ in the y direction. When the spin current reaches the FeMn/Pt interface, depending on the angle between the magnetization $\vec{M}$ of FeMn and $\vec{\sigma}$, a certain portion of the spin current is reflected back into Pt with the remaining traveling across the interface and absorbed by FeMn. The reflection is maximum when $\vec{M} \parallel \vec{\sigma}$ and minimum when $\vec{M} \perp \vec{\sigma}$. The reflected spin current $j_s^{\rm (ref)}$ is converted to a charge current $j_c^{\rm (ISHE)}$ in Pt through the inverse SHE (ISHE) which flows in the opposite direction of the original current j_c. As a consequence, the longitudinal resistance of Pt in the x direction is modulated by the direction of $\vec{M}$, leading to the appearance of SMR given by $R_{xx} = R_0 - \Delta R(\vec{m}\cdot\vec{\sigma})^2$, where R_{xx} is the longitudinal resistance, $\vec{m}$ the unit vector of magnetization, R_0 the isotropic longitudinal resistance, and ΔR the SMR-induced resistance change [36]. As illustrated in Fig. 2(b), the SMR can be readily obtained by measuring R_{xx} under a rotating magnetic field in different coordinate planes, or angle-dependent MR (ADMR) measurements. If the applied field H is sufficiently large to saturate the magnetization, the SMR ratio can be calculated from the relation $\Delta R/R_{xx} = (R_{xx}^z - R_{xx}^y)/R_{xx}^y$, where R_{xx}^z and R_{xx}^y are the longitudinal resistance R_{xx} obtained with H applied in the z and y direction, respectively. The value of SMR and SOT effective field are closely related to each other in the way that SMR (SOT) is minimum (maximum) when $\vec{M} \perp \vec{\sigma}$ and vice versa when $\vec{M} \parallel \vec{\sigma}$. The main difference is that the reflected spin current is converted to SMR through ISHE, whereas the FeMn absorbed spin current is converted to SOT effective field through the magnetic moment in FeMn. Therefore, the observation of clear SMR can further confirm the SOT effect observed in the FeMn/Pt layer (a more quantitative discussion will be presented in Sec. III C).

In addition to Hall bars, coupon films have also been prepared for x-ray diffraction (XRD) and magnetic measurements. The XRD measurements were performed on

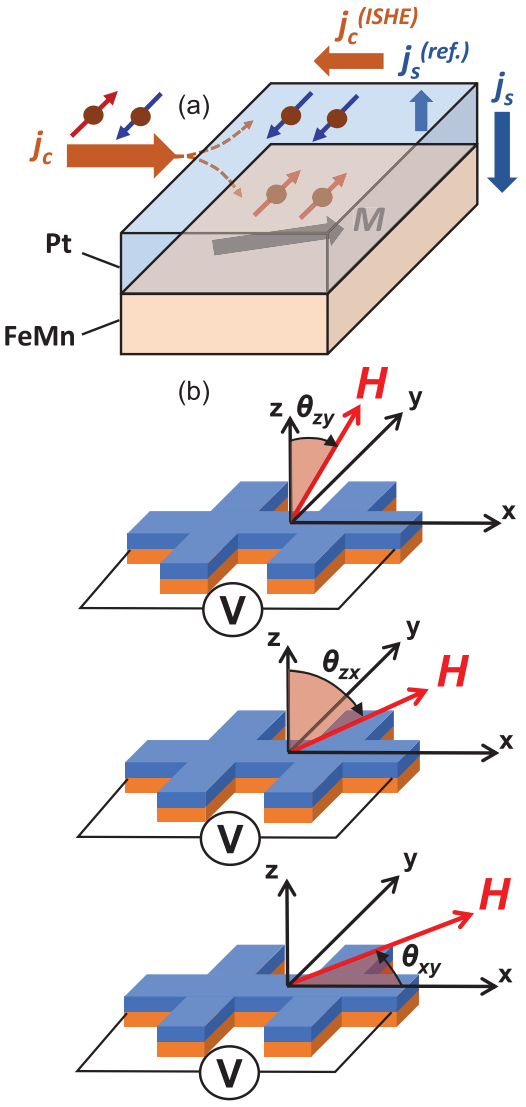

FIG. 2. (a) Schematic of SMR generation mechanism in FeMn/Pt bilayers. (b) Schematic of ADMR measurements with a constant rotating field H in the zy, zx, and xy planes, respectively.

D8-Advance Bruker system with Cu K_α radiation. Magnetic measurements were carried out using a Quantum Design vibrating sample magnetometer (VSM) with the samples cut into a size of 4 × 5 mm. The resolution of the system is better than 6×10^{-7} emu.

III. RESULTS AND DISCUSSION

A. Structural and magnetic properties of FeMn

Figure 3 shows the XRD patterns of coupon films with different structures: (A) Si/SiO_2/Ta(3)/NiFe(3)/FeMn(15)/Ta(3), (B) Si/SiO_2/Ta(3)/FeMn(15)/Ta(3), (C) Si/SiO_2/FeMn(15)/Ta(3), and (D) Si/SiO_2/Ta(3)/NiFe(3)/Ta(3). The Ta capping layer is used to prevent the samples from oxidization. In order to obtain a certain level of signal strength, the thickness of FeMn was intentionally made thicker than those of the samples for electrical transport measurements. As can be seen from the figure, all the samples with a FeMn layer, namely, A, B, and C, exhibit a peak at 43.5°, corresponding

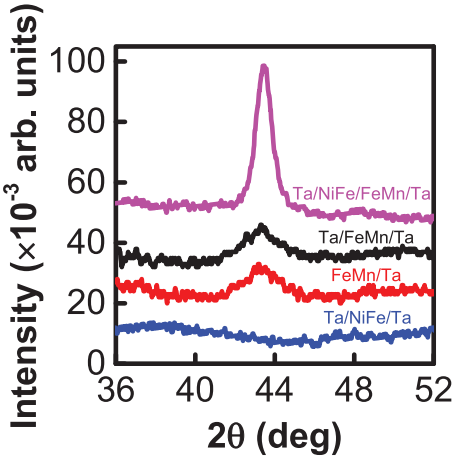

FIG. 3. XRD patterns for Ta(3)/NiFe(3)/FeMn(15)/Ta(3), Ta(3)/FeMn(15)/Ta(3), FeMn(15)/Ta(3), and Ta(3)/NiFe(3)/Ta(3) coupon films. Curves are vertically shifted for clarity.

to the (111) peak of FeMn. This indicates that the FeMn layer is well textured in the [111] direction. The bottom Ta layer enhances the adhesion to the substrate, but it has negligible effect on the texture of FeMn, as shown by the subtle difference between the peak intensities of XRD pattern B and C. Therefore, for electrical measurements, the Ta seed layer can be removed in order to avoid the formation of a dead layer at the Ta/FeMn interface and also to eliminate any current-induced effect from Ta. On the other hand, the insertion of a thin NiFe underlayer significantly enhances the [111] texture of FeMn, as can be seen from the significantly larger peak intensity of A as compared to B and D.

Magnetic measurements were performed on two series of coupon films: (i) a single layer of FeMn(3) covered by different capping layers: Pt(3), Ta(3), and Au(3); and (ii) a single layer of FeMn(t_{FeMn}) with $t_{FeMn} = 1-15$ nm capped by a Pt(3) layer. Figure 4(a) shows the magnetization versus field (M-H) loops for the first set of samples after subtracting the diamagnetic signal from the substrate. All the samples exhibit FM-like M-H curves with a negligible hysteresis but a large saturation field around 20 kOe. The samples capped with Pt and Au show similar M-H loops and saturation magnetization, whereas the samples capped by Ta exhibit an apparently different behavior: both the saturation field and magnetization are much smaller than those of the other two samples. As shown in the inset of Fig. 4(a), the saturation magnetization M_s (averaged over the field range from 20 to 30 kOe) of the Pt-capped sample is slightly higher than that of the Au-capped sample, and both are almost double of that of the Ta-capped sample. This is consistent with earlier reports that (i) Pt interfacial layer can be easily magnetized through proximity effect when contacting with a FM [37,38], but the same type of effect is weak in Au [39] and (ii) Ta can create a magnetic dead layer in the adjacent FM [40]. Similar proximity effect has been observed at FeMn/Pt interfaces in previous studies on exchange bias [41,42]. Obviously, the proximity-effect-induced moment alone is unable to account for the large saturation moment shown in Fig. 4(a). In order to better understand the origin of the observed net moment, VSM measurements were performed on the second series of

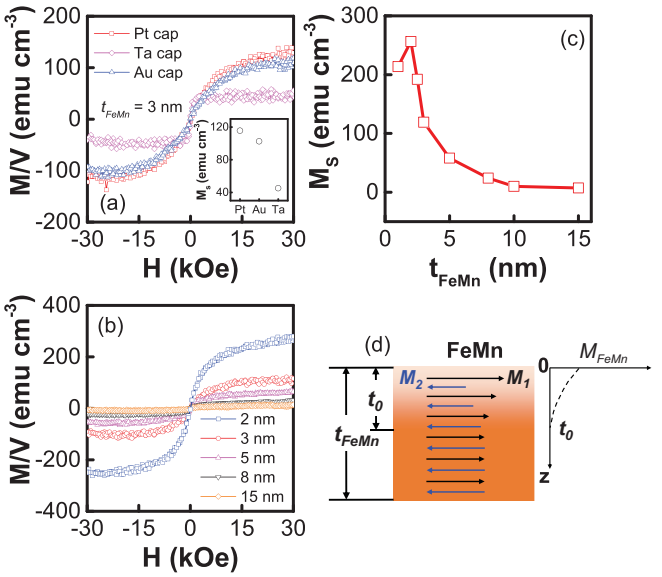

FIG. 4. (a) *M-H* loops for FeMn(3)/Pt(3), FeMn(3)/Ta(3), FeMn(3)/Au(3), respectively. (b) *M-H* loops for FeMn(t_{FeMn})/Pt with $t_{FeMn} = 2, 3, 5, 8$, and 15 nm. (c) FeMn thickness dependence of M_s of FeMn(t_{FeMn})/Pt(3) bilayers. (d) Illustration of spin sublattices with unequal magnetizations in FeMn near the FeMn/Pt interface. Inset of (a): M_s of bilayers with different capping layer.

samples with varying FeMn thicknesses but a fixed Pt-capping layer. Figure 4(b) shows the *M-H* loops of FeMn(t_{FeMn})/Pt(3) with $t_{FeMn} = 2$, 3, 5, 8, and 15 nm, respectively. Although the shape of the *M-H* loops looks quite similar among these samples, the saturation magnetization decreases quickly with increasing t_{FeMn}, and it drops to almost zero at $t_{FeMn} = 8$ nm [see Fig. 4(c)]. This suggests that the observed saturation magnetizations in thin FeMn are mainly due to canting of spin sublattices subject to a large external field. Canting at a moderate field is only possible when the thickness is small due to the reduced sublattice exchange field at small thickness. With the increase of thickness, a bulklike AFM order will eventually be fully established; when this happens, it would be difficult to cause any canting of the spin sublattices at a moderate field, leading to a vanishing saturation magnetization in the FeMn/Pt bilayer. Any residual saturation moment observed in samples with thick FeMn must come from both the proximity-induced moment in Pt and the uncompensated spins from the interfacial layer of FeMn. These net moments are expected to decrease quickly from the interface. However, when t_{FeMn} is below t_0 (the critical thickness for establishing a rigid AFM order at RT), as depicted in Fig. 4(d), the interaction between Pt and FeMn will lead to formation of two spin sublattices with unequal magnetizations. Although the net uncompensated moment is expected to decrease from the interface, for the sake of simplicity, we will assume that it is uniform throughout the FeMn when it is thin.

B. MR of NiFe/FeMn/Pt trilayers

To further correlate the magnetic property of FeMn with the *M-H* loops in Fig. 4, MR measurements were performed on NiFe(3)/FeMn(t_{FeMn})/Pt trilayer Hall bars with t_{FeMn} varying

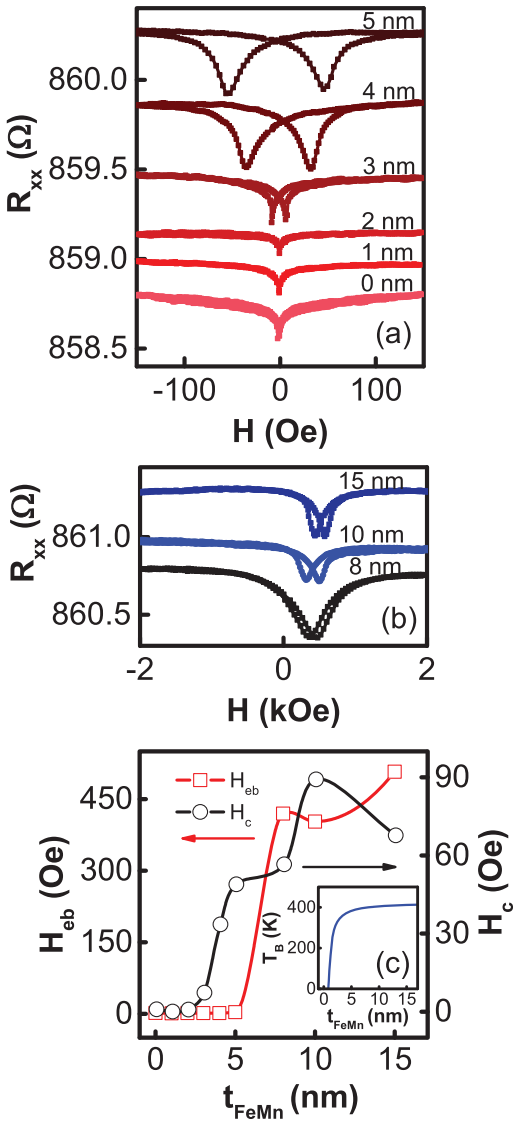

FIG. 5. (a) MR curves for NiFe(3)/FeMn(t_{FeMn})/Pt trilayers with $t_{FeMn} = 0-5$ nm. (b) MR curves for NiFe(3)/FeMn(t_{FeMn})/Pt trilayers with $t = 8-15$ nm. (c) Dependence of H_c and H_{eb} on t_{FeMn} extracted from (a) and (b). Inset of (c): t_{FeMn} dependence of T_B (reproduced from Ref. [44]).

from 0 to 15 nm. Figures 5(a) and 5(b) show the MR curves for samples with t_{FeMn} in the range of 0–5 nm and 8–15 nm, respectively. Since the MR from NiFe is significantly larger than that of FeMn, we can safely assume that the MR is dominated by the signal from NiFe for all the samples, regardless of the FeMn thickness. Shown in Fig. 5(c) are the coercivity of NiFe(H_c) and exchange bias field (H_{eb}) at the NiFe/FeMn interface extracted from the MR curves in Figs. 5(a) and 5(b). As can be seen from the results, the effect of FeMn on NiFe depends strongly on its thickness. For $t_{FeMn} < 2$ nm, there is neither H_c enhancement of NiFe nor observable H_{eb} at the NiFe/FeMn interface. This indicates that, in this thickness region, the blocking temperature (T_B) and possibly Neel temperature (T_N) of the magnetic grains are below RT. In other words, the spin sublattices within each grain are weakly coupled, and the entire film behaves more or

less like a superpara-AFM. At t_{FeMn} of 3–5 nm, an increased H_c (around 8–270 Oe) and a small H_{eb} (around 1–3 Oe) were observed, suggesting the formation of AFM order ($T_N > T_B >$ RT) as the thicknesses increases. In this case, the exchange coupling between the spin sublattices should have already been established in most of the grains, though its strength as well as the anisotropy remains small and varies among the different grains. Therefore, in this thickness region, the FeMn layer may be treated as an AFM with a finite distribution of exchange coupling strength and anisotropy, with both having a small magnitude. As a consequence, the AFM sublattices can be canted by an external magnetic field with a moderate strength, as shown in Figs. 4(a) and 4(b). The onset of a clear exchange bias, with the H_{eb}(~450 Oe) comparable to typical values reported in the literature [43], was observed for samples with $t_{FeMn} > 8$ nm. In this thickness range, the variation in exchange coupling among the grains may be ignored, and the entire film can be treated as an AFM with a uniform exchange coupling strength, but having a finite distribution of anisotropy. As reproduced in the inset of Fig. 5(c), the observed thickness dependence of the AFM order in our FeMn film is consistent with the previous theoretical calculation [44] of the thickness dependence of T_B. It should be noted that the critical thickness for onset of clear exchange bias coincides with the thickness above, which the saturation magnetization drops to a minimum in Figs. 4(b) and 4(c). This further affirms our explanation that the large saturation moments observed in thin FeMn are due to canting of the spin sublattices. As will be presented shortly, the current-induced PHE signal also vanishes as the thickness of FeMn exceeds the critical thickness in both bilayer and trilayer samples. Therefore, we focus the discussion hereafter mainly on ultrathin FeMn films (1–5 nm). Although the FeMn layers in this thickness range are not normal AFM in the strict sense, the improved response of AFM spins to external field provides a convenient way to study the interaction of AFM with spin current.

C. PHE measurements of FeMn/Pt bilayers

We now turn to the PHE measurement results of FeMn(t_{FeMn})/Pt(3) bilayer samples. The measurement geometry is shown in Fig. 6(a). Shown in Fig. 6(b) are the planar Hall resistance (ΔR_{xy}) versus field (H) curves obtained at different bias currents (I), for the $t_{FeMn} = 3$ nm sample. Here, the Hall resistance is given by $\Delta R_{xy} = [V_{xy}(+I,H) + V_{xy}(-I,H)]/2I$, which represents the change in Hall resistance caused by the current-induced effective field. As can be seen from Fig. 6(b), the overall shape of the PHE curves resembles that of a typical FM. The Hall signal is weak at low bias current and increases prominently with increasing the bias current. Moreover, the peak position of PHE shifts to larger field values as the bias current increases. Since the AFM consists of grains with randomly distributed in-plane anisotropy axes, the PHE signal can be understood as resulting from two competing fields, i.e., the externally applied field in the x direction and current-induced effective field in the y direction, acting on the spin sublattices of FeMn. The increase of PHE signal amplitude and shift of the peak position can be understood as being caused by the increase of H_I when the current

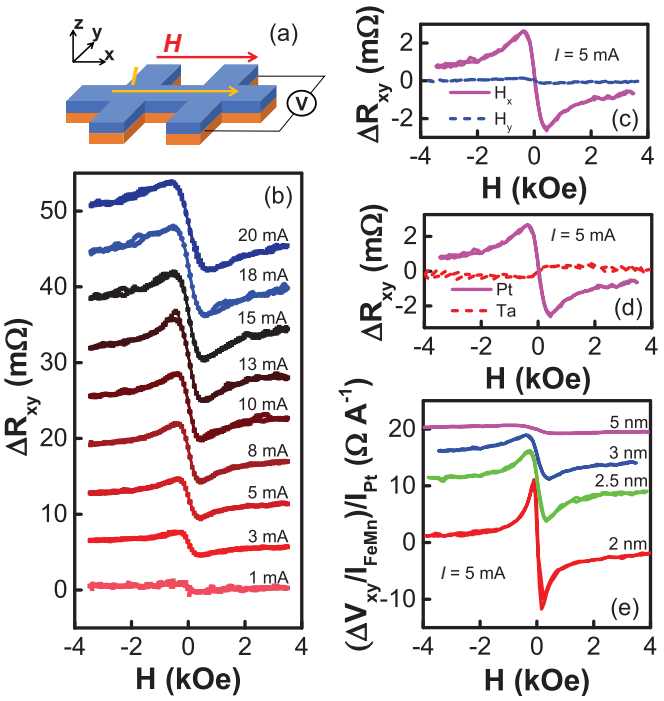

FIG. 6. (a) Schematic of PHE measurement at different bias currents. (b) PHE curves for FeMn(3)/Pt(3) at different bias currents. (c) PHE curves for FeMn(3)/Pt(3) obtained at 5 mA with field swept in the x and y direction, respectively. (d) A comparison of PHE curves at 5 mA for FeMn(3)/Ta(3) (dashed line) and FeMn(3)/Pt(3) (solid line) with the field applied in the x direction. (e) Normalized PHE curves for samples with different FeMn thickness from 2–5 nm. Note that curves in (b) and (e) are vertically shifted for clarity.

increases. The role of H_I is confirmed by the observation that the PHE signal vanishes when the field is swept in the y direction, as shown in Fig. 6(c) for a bias current of 5 mA. To further demonstrate that H_I indeed originates from the SHE, we fabricated a Si/SiO_2/FeMn(3)/Ta(3) control sample. Figure 6(d) shows the comparison of the PHE curves at 5 mA for both FeMn(3)/Ta(3) and FeMn(3)/Pt(3) samples. A similar FM-like PHE signal is observed in FeMn/Ta, except that the magnitude is much smaller, and its polarity is opposite to that of FeMn/Pt. The latter implies that the sign of H_I in FeMn/Ta is opposite to that of FeMn/Pt, which is consistent with the opposite sign of θ_{SH} for Pt and Ta. It can also be inferred from the results that Joule heating is not the major cause for the observation because, otherwise, one would expect a PHE with the same polarity in both FeMn/Pt and FeMn/Ta as the temperature gradient is not likely to change direction upon changing the top layer, as both Pt and Ta have a lower resistivity as compared to FeMn. The bias current dependence of PHE for samples with different FeMn thickness is similar to the one shown in Fig. 6(b) except that its magnitude decreases with increasing the FeMn thickness. Figure 6(e) shows the FeMn thickness dependence of PHE voltage. To have a meaningful comparison, instead of showing the nominal Hall resistance by dividing the Hall voltage by the total current, we show the Hall voltage scaled by the currents in both the FeMn (I_{FeMn}) and Pt (I_{Pt}) layers. This makes sense because the PHE signal mainly comes from the FeMn layer, but its

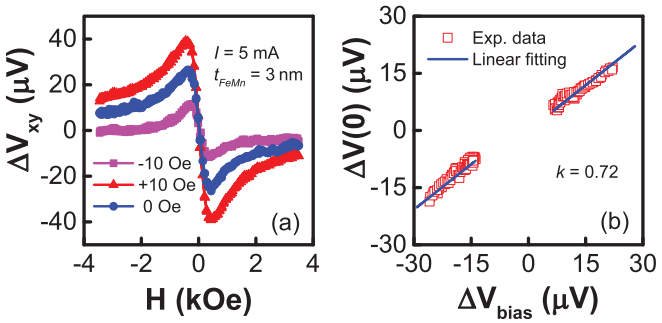

FIG. 7. (a) PHE curves for the FeMn(3)/Pt(3) bilayer measured at 5 mA with different transverse bias field (0, +10, and −10 Oe). (b) Linear fitting of $\Delta V_{xy}(0)$ against $\Delta V_{\rm bias} = [\Delta V_{xy}(H_{\rm bias} = 10\,{\rm Oe}) - \Delta V_{xy}(H_{\rm bias} = -10\,{\rm Oe})]$ to determine the ratio of the current-induced H_I to $2H_{\rm bias}$.

amplitude is determined by the current-induced field (H_I) from the Pt layer. Here, $I_{\rm FeMn}$ and $I_{\rm Pt}$ were calculated using three-dimensional (3D) finite element analysis by using the experimentally derived resistivity values for different layers given in Sec. II. To shorten the simulation time, the Hall bar sample was scaled down to a strip with a length of 2 μm, a width of 0.2 μm, and the thicknesses of each layer remained the same as the actual samples. As can be seen from Fig. 6(e), the PHE signal decreases with increasing the FeMn thickness, and it becomes vanishingly small at thicknesses above 8 nm (not shown here). This is in good agreement with the results of both the VSM and MR measurements, as discussed above. In other words, the PHE signal observed in FeMn/Pt bilayers are caused by the current-induced canting of spin sublattices with unequal magnetizations. The signal gradually decreases to zero as the AFM hardens with increasing the thickness.

In order to quantify the strength of H_I, we carried out the second-order PHE measurements as described in Sec. II. Figure 7(a) shows an example of one set of PHE curves with $H_{\rm bias} = 0$, +10, and −10 Oe, respectively, at a bias current of 5 mA for the FeMn(3)/Pt(3) sample. As can be seen, the PHE signal magnitude changes with the total field in the y direction, including both H_I and $H_{\rm bias}$. The increase of PHE at $H_{\rm bias} = +10$ Oe indicates that H_I is in the positive y direction. Figure 7(b) shows the linear fitting of $\Delta V_{xy}(0)$ against $\Delta V_{\rm bias} = [\Delta V_{xy}(+10\,{\rm Oe}) - \Delta V_{xy}(-10\,{\rm Oe})]$ using the data in Fig. 7(a). For a better linear approximation, the data at low fields were excluded, and only the data at fields above ±1 kOe were used for the fitting [10]. Here, H_I can be calculated from the slope k by using the relation $H_I = 2kH_{\rm bias}$. The offset between the fitting lines at positive and negative regions is understood to be caused by either $H_{\rm DL}$ or the thermal effect [10,12]. The small amplitude of the offset confirms again that the contributions from both effects are small in the PHE signals obtained from the FeMn/Pt bilayers. The same experiments have been repeated for FeMn/Pt bilayers with different FeMn thickness ($t_{\rm FeMn} = 2$–5 nm), and the results are shown in Fig. 8(a). As can be seen, the H_I in all samples scales almost linearly with the bias current. After subtracting the Oersted field ($H_{\rm Oe}$), the effective field ($H_{\rm FL}$) normalized to the current density in Pt is shown in Fig. 8(b). The Oersted field in the FeMn layer is calculated using 3D finite element analysis on scaled down strips with a dimension of 20 × 2 μm. The calculated Oersted field ($H_{\rm Oe}$) (also normalized to the current density in Pt) on the order of 1×10^{-7} Oe (A^{-1} cm^2) is almost independent of the FeMn thickness and is much smaller than the measured H_I for all samples. As shown in Fig. 8(b), the $H_{\rm FL}/j_{\rm Pt}$ ratio (open square) is in the range of 2.05×10^{-5} to 2.44×10^{-5} Oe (A^{-1} cm^2) for FeMn/Pt bilayers; this is nearly two orders of magnitude larger than that of the NiFe/Pt control sample [4.01×10^{-7} Oe (A^{-1} cm^2)]. Although the physical origin of the fieldlike effective field in FM/HM bilayers is still debatable, recent studies suggest that it can be written in the following form by taking into account the spin Hall current from the HM layer only [45,46]:

$$H_{\rm FL}/j_c = \frac{\hbar}{2e}\frac{\theta_{\rm SH}}{M_s t_{\rm FM}}\left(1 - \frac{1}{\cosh(d/\lambda_{\rm HM})}\right) \times \frac{g_i}{(1+g_r)^2 + g_i^2}, \quad (1)$$

where $g_r = {\rm Re}[G_{\rm mix}]\rho\lambda_{\rm HM}\coth(d/\lambda_{\rm HM})$, $g_i = {\rm Im}[G_{\rm mix}]\rho\lambda_{\rm HM}\coth(d/\lambda_{\rm HM})$ with $G_{\rm mix}$ the spin-mixing conductance of the FM/HM interface, ρ the resistivity of HM, and $\lambda_{\rm HM}$ the spin diffusion length in HM. The spin Hall origin of the fieldlike effective field is supported by several experimental studies [7,11,12,14], especially when the FM layer is thick, based on the observation that the field directions are opposite to each other in Pt- and Ta-based FM/HM bilayers with the same

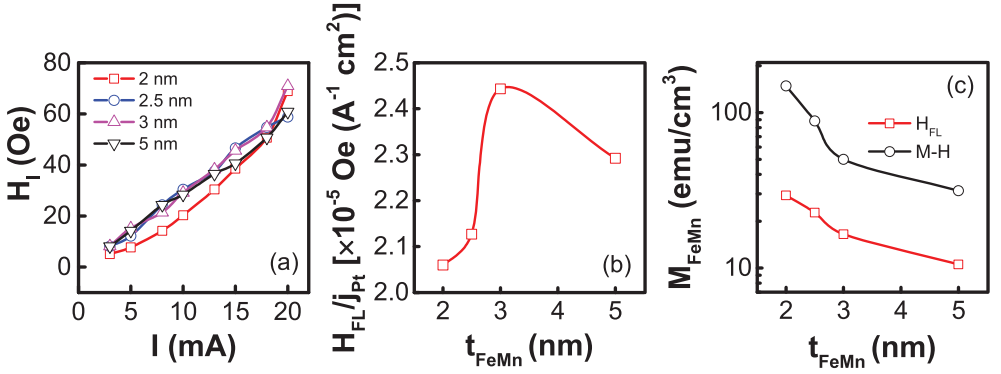

FIG. 8. (a) Extracted H_I for FeMn($t_{\rm FeMn}$)/Pt(3) bilayers with $t_{\rm FeMn} = 2$–5 nm. (b) $H_{\rm FL}/j_{\rm Pt}$ (open square) as a function of $t_{\rm FeMn}$ after subtracting the Oersted field. (c) $M_{\rm FeMn}$ calculated from $H_{\rm FL}$ using Eq. (1) (open square) and $M_{\rm FeMn}$ extracted from the M-H loops at 4 kOe (open circle). Note that the data in (c) is plotted in log scale for clarity.

FM. Following this scenario, the large effective field obtained in this paper can be readily understood by substituting the relevant parameters into Eq. (1). These include the moment per unit area in NiFe($M_s t_{\mathrm{NiFe}}$) and FeMn (M_{FeMn} t_{FeMn}) and spin-mixing conductance (G_{mix}) at the NiFe/Pt and FeMn/Pt interfaces. If we assume a same G_{mix} for the two types of interfaces and use the known M_s of NiFe of 800 emu cm^{-3}, the resultant net magnetization of FeMn, M_{FeMn}, is in the range of 10.5−29.3 emu cm^{-3} with a thickness of 2–5 nm, as shown in Fig. 8(c) (open square). Also shown in Fig. 8(c) (open circle) is the average magnetization extracted from the *M-H* curves shown in Fig. 4(b) at an applied field of 4 kOe (note: we use the magnetization at 4 kOe instead of the saturation magnetization because the maximum applied field in electrical measurements was 4 kOe). As can be seen from the figure, although the net magnetization from *M-H* loops is around five times larger than that calculated from the H_{FL}, both show a very similar trend as long as FeMn thickness dependence is concerned. The difference in absolute values is understandable because, in electrical measurements, the magnetic moment that affects H_{FL} is mainly concentrated at the FeMn/Pt interface, whereas the VSM measurement detects the moment of the entire film. These results suggest that the small net moment is the determining factor that gives the large effective field-to-current ratio as compared to NiFe.

As shown in Fig. 8(b), the electrically derived $H_{\mathrm{FL}}/j_{\mathrm{Pt}}$ ratio (open square) increases sharply with FeMn thickness below 3 nm and then decreases slowly as t_{FeMn} increases further. This is in sharp contrast with the monotonically decreasing dependence of H_{FL} on FM thickness (t_{FM}) in typical FM/HM heterostructures [12,47]. The latter is due to the fact that, when t_{FM} increases, the product of t_{FM} and M_{FM} increases accordingly, leading to a $1/t_{\mathrm{FM}}$ dependence of H_{FL}. However, in the case of FeMn/Pt bilayers, the net magnetization M_{FeMn} decreases with t_{FeMn} (>2 nm), as confirmed by the VSM measurement results shown in Fig. 8(c). This naturally leads to a peak in the curve in Fig. 8(b). The peak position of H_{FL} agrees well with the region where H_c is enhanced, but clear exchange bias has yet to be established [see Fig. 5(c)]. This suggests that the enhancement of H_{FL} occurs in the region that AFM order is just about to form, and their spin sublattices can still be canted easily by either an external or effective field. We noticed that, in early theoretical work on spin torque in AFM, H_{FL} is treated as negligibly small [48,49]. This is valid for rigid AFM systems. It should be pointed out that our results presented in Figs. 6–8 do not contradict these reports because the H_{FL} indeed vanishes when the FeMn thickness is above 8 nm. At such a thickness, a rigid AFM order is formed, and any H_{FL} on the spin sublattices should have been cancelled out.

To further confirm the SOT effect in FeMn/Pt and verify the nonmonotonic thickness dependence of the effective field, we performed the ADMR measurements in the bilayer samples with $t_{\mathrm{FeMn}} = 2-5$ nm using the schematic shown in Fig. 2(b). Figure 9(a) shows the ADMR results for a FeMn(3)/Pt(3) bilayer measured at a constant field of 30 kOe rotating in the xy, zx, zy planes, respectively. The almost overlapping between θ_{zy} and θ_{xy} dependence of MR indicates that the conventional anisotropic MR in FeMn/Pt is negligibly small, and the MR measured is dominated by SMR. The SMR ratio on the order of 10^{-3} is comparable to that in NiFe/Pt reported earlier [50]

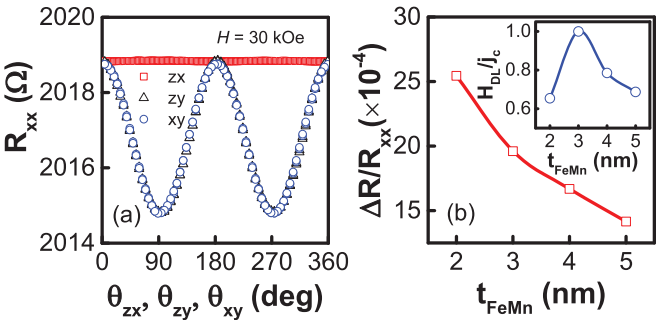

FIG. 9. (a) ADMR results at 30 kOe for FeMn(3)/Pt(3) bilayer. (b) Thickness dependence of SMR ratio $\Delta R/R_{xx}$ with $t_{\mathrm{FeMn}} = 2-5$ nm. Inset of (b): Normalized thickness dependence of antidampinglike effective field calculated from Eq. (4).

and much larger than that in the YIG/Pt system [36]. Figure 9(b) shows the SMR ratio as a function of FeMn thickness in the range $t_{\mathrm{FeMn}} = 2-5$ nm, which decreases monotonically as the FeMn thickness increases, suggesting the decrease of spin current entering the FeMn layer. To have a quantitative correlation of this thickness dependence to that of H_{DL}, one needs to look into their expressions, respectively. Firstly, the SMR ratio can be expressed as [34,46]

$$\frac{\Delta R}{R_{xx}} = {\theta_{\mathrm{SH}}}^2 \frac{\lambda_{\mathrm{Pt}}}{d_{\mathrm{Pt}}} \frac{\tanh(d_{\mathrm{Pt}}/2\lambda_{\mathrm{Pt}})}{(1+\xi)} \left(1 - \frac{1}{\cosh(d_{\mathrm{Pt}}/\lambda_{\mathrm{Pt}})}\right) \times \frac{g_r(1+g_r)+{g_i}^2}{(1+g_r)^2+{g_i}^2}, \tag{2}$$

where $\xi = \rho_{\mathrm{Pt}} t_{\mathrm{FeMn}}/\rho_{\mathrm{FeMn}} d_{\mathrm{Pt}}$ is introduced to take into account the current-shunting effect by FeMn, and $\rho_{\mathrm{Pt}}(\rho_{\mathrm{FeMn}})$ and $d_{\mathrm{Pt}}(t_{\mathrm{FeMn}})$ are the resistivity and thickness of Pt (FeMn), respectively. On the other hand, the antidampinglike effective field H_{DL} can be written as [45,46]

$$H_{\mathrm{DL}}/j_c = \frac{\hbar}{2e} \frac{\theta_{\mathrm{SH}}}{M_s t_{\mathrm{FeMn}}} \left(1 - \frac{1}{\cosh(d_{\mathrm{Pt}}/\lambda_{\mathrm{Pt}})}\right) \times \frac{g_r(1+g_r)+{g_i}^2}{(1+g_r)^2+{g_i}^2}. \tag{3}$$

The combination of Eqs. (2) and (3) gives

$$H_{\mathrm{DL}}/j_c = \frac{\hbar}{2e} \frac{1}{\theta_{\mathrm{SH}} M_s t_{\mathrm{FeMn}}} \frac{d_{\mathrm{Pt}}}{\lambda_{\mathrm{Pt}}} \frac{1}{\tanh(d_{\mathrm{Pt}}/2\lambda_{\mathrm{Pt}})} \frac{\Delta R}{R_{xx}}. \tag{4}$$

Note that we have set $\xi = 0$ in Eq. (4) since the current-shunting effect taken into account in the calculation of SMR has nothing to do with the reflection/transmission of spin current at the FeMn/Pt interface, or in any case, it is much smaller than unity due to the large difference in resistivity between Pt and FeMn. In this way, the thickness dependence of H_{DL}/j_c can be readily calculated from Eq. (4) by using the thickness dependence of SMR obtained in Fig. 9(b). The inset of Fig. 9(b) shows the normalized FeMn thickness dependence of the antidampinglike effective field calculated from Eq. (4). Note that, ideally, we should use the moment of FeMn at the interface only for M_{FeMn} t_{FeMn}. However, as it is difficult to extract the interface moment independently, we used the volumetric M_{FeMn} instead, which was obtained by the VSM

measurement in Fig. 8(c). Although it is not exactly the same, the thickness dependence of H_{DL} is indeed similar to the FeMn thickness dependence of H_{FL} presented in Fig. 8(b). Therefore, from the results obtained by second-order PHE and ADMR measurements, we demonstrated clearly the existence of SOT effect in FeMn/Pt and the nonmonotonic dependence of the SOT effective field on FeMn thickness.

D. Macrospin model of the FeMn layer

In order to have a more quantitative understanding of the *M-H* loops in Fig. 4(b) and PHE curves in Fig. 6(b) for the FeMn/Pt bilayers, we have simulated both curves using the macrospin model. Although the spin state of bulk FeMn can take either a collinear or noncollinear configuration [51–54], the spin configuration in an ultrathin film may differ from that of the bulk, especially when it interacts with FM or HM like Pt. In the case of the FeMn/FM bilayer, it has been observed experimentally that the spin axis of FeMn is aligned to that of the FM layer from the interface [55–57]. In the case of FeMn/Pt bilayers, the situation can be more complicated due to the strong SO interaction of Pt. Determination of the exact spin configuration is beyond the scope of this paper, which certainly deserves further investigations. However, in order to simplify the problem yet without compromising the underlying physics, we treat the ultrathin FeMn layer as consisting of two collinear spin sublattices with unequal saturation magnetizations M_s. As we will show in this section, the good agreement between experimental and simulation results supports the collinear model. Under this assumption, the *M-H* loops and PHE curves of FeMn/Pt bilayers shown previously can be simulated through energy minimization. Based on the coordinate notation in Fig. 10(a), the free energy density E of a specific grain in the FeMn layer can be written as [58]

$$E = J|\vec{M}_1||\vec{M}_2|\cos(\theta_1-\theta_2) - H[|\vec{M}_1|\cos(\varphi-\theta_1) + |\vec{M}_2|\cos(\varphi-\theta_2)] + K_u(\sin^2\theta_1+\sin^2\theta_2), \quad (5)$$

where J is the sublattice exchange coupling constant, $|\vec{M}_1|$ and $|\vec{M}_2|$ are the magnitude of $\vec{M}_1$ and $\vec{M}_2$, respectively, θ_1 and θ_2 are the angles of $\vec{M}_1$ and $\vec{M}_2$ with respect to the y direction, respectively, φ is the angle between the y direction and H, and K_u is the uniaxial anisotropy constant. Equation (5) can be solved numerically to find the steady-state values for θ_1 and θ_2, which in turn can be used to calculate the *M-H* curve. To facilitate the discussion, we introduce the following parameters: $N = |\vec{M}_1|/|\vec{M}_2|$, $H_A = K_u/|\vec{M}_2|$, and $H_{ex} = J|\vec{M}_2|$. Note that Eq. (5) applies to a single grain with a specific anisotropy axis and exchange coupling strength. Considering the polycrystalline nature of the sample, ideally one should simulate the average *M-H* curve by taking into account the finite distribution of anisotropy axes and exchange field. However, it is found that the calculated curve with a fixed anisotropy axis at 0° is very similar to the one that is obtained by assuming that the anisotropy axes are distributed from 0°–90° at a step of 10° and then taking an average of the calculated curves at different angles. This is due to the fact that

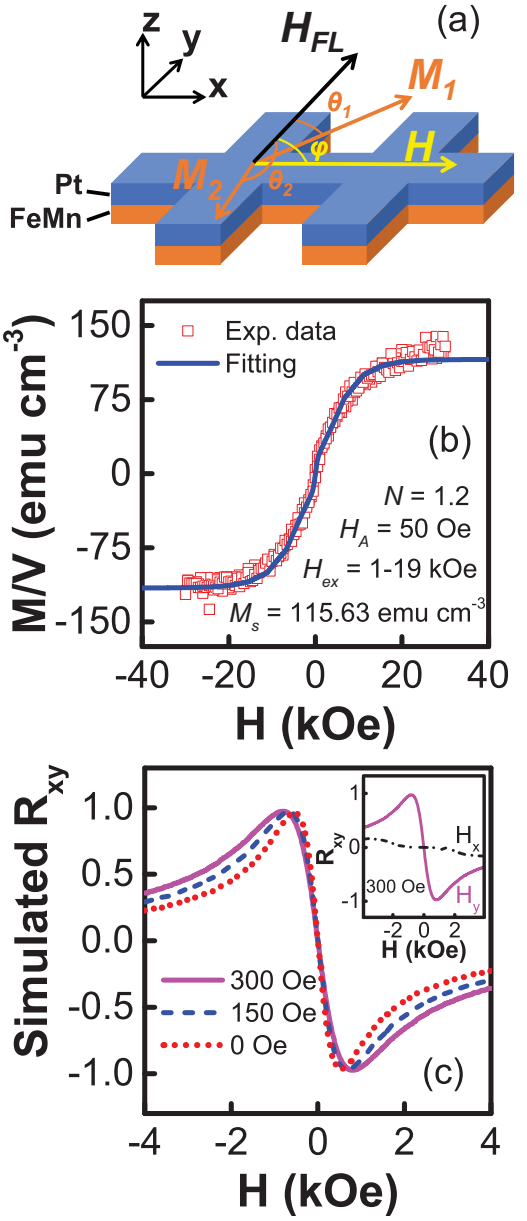

FIG. 10. (a) Illustration of the FeMn spin sublattice configuration, external field, and current-induced H_{FL}. (b) *M-H* loop fitting using the macrospin model for FeMn(3)/Pt(3). (c) Simulated PHE curves with different H_{FL} values (0, 150, and 300 Oe). Inset of (d): Simulated PHE curves at H_{FL} = 300 Oe with the external field applied in the x and y direction, respectively.

K_u in ultrathin FeMn is small, and its effect on steady-state magnetization direction is overtaken by the current-induced effective field. Therefore, for simplicity, in the subsequent simulations, we assumed that the uniaxial anisotropy is along the y axis for all the grains. A log-normal distribution was adopted to account for the exchange field (H_{ex}) distribution: $f(H_{ex}) = \frac{1}{H_{ex}\sigma\sqrt{2\pi}}\exp[-\frac{(\ln H_{ex}-\mu)^2}{2\sigma^2}]$, with $\mu = \log(5000)$, and $\sigma = 0.5$ when H_{ex} is in unit of Oersted. This is justifiable because the grain size of sputtered polycrystalline films typically follows the lognormal distribution [59], and the AFM order is found to enhance with the increase of grain size [60]. The average *M-H* curve was obtained by assuming H_{ex} in the

range of 1–19 kOe with a step of 2 kOe. As can be seen from Fig. 10(b), a reasonably good agreement is obtained between the simulated (solid line) and experimental *M*-*H* curves for the $t_{\mathrm{FeMn}} = 3$ nm sample by assuming $N = 1.2$, $H_A = 50$ Oe, and $M_s = 115.83$ emu cm^{-3}. Next, we proceed to account for the spin current in the sample by introducing in Eq. (5) an additional Zeeman energy term arising from H_{FL}, i.e. $-H_{\mathrm{FL}}(|\vec{M}_1|\cos\theta_1 + |\vec{M}_2|\cos\theta_2)$. Similarly, θ_1 and θ_2 are determined numerically at different H_{FL} values, which in turn are used to calculate the normalized PHE signal at different H: $\mathrm{PHE} = (|\vec{M}_1|\sin 2\theta_1 + |\vec{M}_2|\sin 2\theta_2)/(|\vec{M}_1| + |\vec{M}_2|)$. Figure 10(c) compares the simulated curves at different H_{FL} values with the field in the x direction. The simulated curve resembles a typical PHE curve for a FM, and the peak position increases with increasing H_{FL}, both of which agree well with experimental PHE curves obtained at different bias currents. As shown in the inset of Fig. 10(c), when the field is changed to the y direction, a vanished PHE is obtained. Therefore, the macrospin model is able to account for the main experimental observations in FeMn/Pt bilayers. This strongly supports our arguments that the large fieldlike SOT in FeMn/Pt bilayers is caused by the relatively small magnetic moment in the FeMn, and resultant SOT is able to induce canting of the spin sublattices of the AFM.

Before ending this section, we would like to comment on the validity of the macrospin model. Although the films are polycrystalline, we argue that the macrospin model is able to capture the essential physics of current-induced SOT in FeMn/Pt bilayers because, unlike the charge current which flows in the lateral direction (i.e., the x direction), the spin current generated from Pt flows mainly in the z direction (i.e., in the sample normal direction). Since the FeMn thickness in the samples under investigation (2–5 nm) is comparable to the grain size, we can safely assume that the spin current is confined mostly inside a single crystal grain with negligible influence from the grain boundaries (different from the laterally flowing charge current). Therefore, as long as the polycrystalline film has a well-defined texture in the thickness direction, which is the case in this study, it would appear locally as a "quasisingle crystal" to the vertically flowing spin current. Compared to the true single crystal case, the only difference is that, in the polycrystalline case, the SOT effect is further averaged over different grains due to the random distribution of crystalline anisotropy and exchange energy, which has been taken into account in the above discussion. Therefore, we believe the macrospin model is appropriate for interpretation of the experimental results observed in this paper.

E. PHE measurements of NiFe/FeMn/Pt trilayers

To further demonstrate that the spin current generated in Pt is indeed largely absorbed by FeMn, we have fabricated NiFe(3)/FeMn(t_{FeMn})/Pt(3) trilayer Hall bars and studied SOT-induced magnetization rotation in NiFe. Figure 11(a) shows the PHE curves at different bias currents (I) for the NiFe(3)/FeMn(3)/Pt(3) sample. Similar to the results shown in Fig. 6(b), the PHE signal increases prominently as I increases, indicating the presence of a current-induced effective field H_I in the y direction. The Hall signal is much larger than that

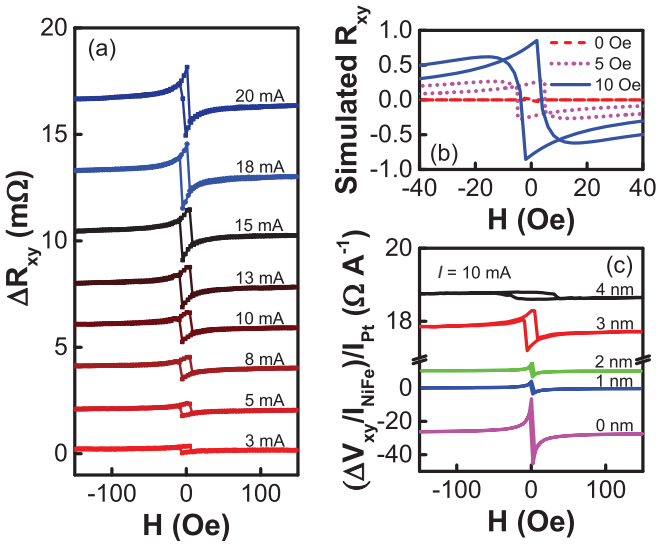

FIG. 11. (a) PHE curves at different bias currents for the NiFe(3)/FeMn(3)/Pt(3) trilayer. (b) Simulated PHE curves with 0, 5, and 10 Oe bias field in the y direction. (c) Normalized PHE curves at 10 mA for the trilayer sample with FeMn thicknesses of 0–4 nm. Note that the curves in (a) and (c) are vertically shifted for clarity.

of the FeMn/Pt bilayer in the same field range; therefore, the signal from the trilayer is dominantly from the NiFe layer. The results can be qualitatively understood as follows. The spin current generated by the Pt layer travels through the FeMn spacer and induces SOT in the NiFe layer. The SOT will then cause a rotation of the NiFe magnetization, leading to the observed increase of PHE with the bias current. To have a more quantitative understanding of the current dependence of PHE signal, 3D micromagnetic modeling was performed on a NiFe element with and without a transverse field using OOMMF [61]. To shorten the computation time, in the simulation, the sample is scaled down to a strip with a dimension of 23 μm × 2 μm × 3 nm. The parameters used are: saturation magnetization $M_s = 8 \times 10^5$ A m^{-1}, exchange constant $J = 1.3 \times 10^{-11}$ J m^{-1}, damping constant $\alpha = 0.5$, anisotropy constant $K_u = 100$ J m^{-3}, and unit cell size 10 × 10 × 3 nm. A fixed bias field in the y direction is used to simulate the effective field induced by the current. To account for the Hall measurement geometry, only the data at the center area of 1 × 2 μm, representing the Hall bar cross, is taken into consideration for the calculation of the PHE signal. Figure 11(b) shows the simulated PHE curves at bias fields of 0, 5, and 10 Oe, respectively. Note that, due to the much smaller size used in the simulation, the simulated H_c is much larger than the measured value, and therefore, a large transverse bias field of 10 Oe was used in the simulation accordingly. Except for the large H_c, the simulated curves resemble well the measured PHE curves. Figure 11(c) shows the normalized PHE curves for samples with different FeMn thicknesses at a bias current of 10 mA. As can be seen, the signal amplitude decreases as the thickness increases, indicating the decrease of the H_I at larger FeMn thickness. When the FeMn thickness exceeds 5 nm, the signal becomes vanishingly small, suggesting that the spin current cannot travel through the FeMn layer beyond this thickness.

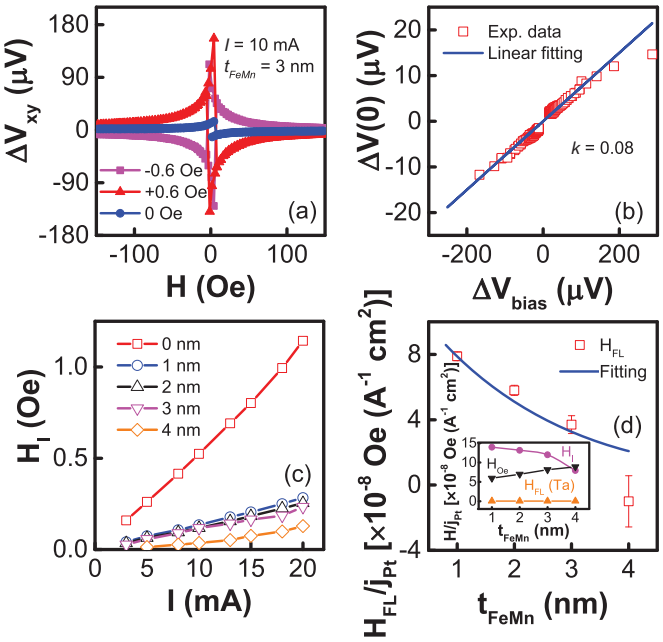

FIG. 12. (a) PHE curves for the NiFe(3)/FeMn(3)/Pt(3) trilayer measured at 10 mA with different transverse bias field (0, +0.6, and −0.6 Oe). (b) Linear fitting of $\Delta V_{xy}(0)$ against $\Delta V_{\rm bias} = [\Delta V_{xy}(H_{\rm bias} = 0.6\,{\rm Oe}) - \Delta V_{xy}(H_{\rm bias} = -0.6\,{\rm Oe})]$ to determine the ratio of the current-induced H_I to $2H_{\rm bias}$. (c) Extracted H_I for samples with $t_{\rm FeMn} = 0$–4 nm. (d) Experimental values for H_I (open square) and fitting using Eq. (8) (solid line). Inset of (d): FeMn thickness dependence of H_I (circle), $H_{\rm Oe}$ in NiFe (down triangle), and $H_{\rm FL}$ from Ta (upper triangle), respectively. Note that the data in (d) are normalized to the current density in Pt.

To quantity the strength of the fieldlike effective field in the NiFe layer, again we carried out the second-order PHE measurements. Figure 12(a) shows one set of PHE curves for NiFe(3)/FeMn(3)/Pt(3) obtained with $I = 10$ mA, and $H_{\rm bias} = 0$, $+0.6$, and -0.6 Oe, respectively. The flip of curve polarity at positive and negative bias field suggests that H_I is comparable to the applied bias field of 0.6 Oe. Figure 12(b) shows the linear fitting of $\Delta V_{xy}(0)$ against $\Delta V_{\rm bias}$ using the data in Fig. 12(a). The slope k turns out to be much smaller than that obtained for the FeMn/Pt bilayers, as shown in Fig. 7(b). This in turn gives a much smaller H_I for the trilayer samples with $t_{\rm FeMn} = 0$–4 nm, as shown in Fig. 12(c). Similar to the case of FeMn/Pt bilayers, H_I for all samples scales almost linearly with the bias current. The $t_{\rm FeMn} = 0$ sample corresponds to a Ta(3)/NiFe(3)/Pt(3) trilayer. The obtained H_I value of 0.52 Oe at a bias current of 10 mA is comparable to the reported value for a similar structure [12]. The H_I value drops sharply with the insertion of a 1 nm FeMn, and decreases further as the FeMn thickness increases. To quantify the current contribution directly from the Pt layer, we have to subtract from H_I two other contributions, i.e., $H_{\rm Oe}$ in the NiFe layer and $H_{\rm FL}$ from the Ta seed layer. The total Oersted field in NiFe, $H_{\rm Oe}$, is calculated using 3D finite element analysis, and the results are shown in the inset of Fig. 12(d) as a function of FeMn thickness (down triangle); it increases with FeMn thickness due to the increase of current in the FeMn layer. In order to estimate the contribution of current in the Ta layer to H_I, we have fabricated a NiFe(3)/Ta(3) control sample and measured the effective field using the same second-order PHE measurement. The effective field-to-current ratio obtained is $H_{\rm FL}({\rm Ta})/j_{\rm Ta} = 1.49 \times 10^{-7}\,{\rm Oe\,(A^{-1}cm^2)}$. Based on this value, we can estimate the contribution of Ta current in the trilayers with different FeMn thicknesses. The results are shown in the inset of Fig. 12(d) in upper triangles. The value of $H_{\rm FL}$(Ta) is almost constant due to the much larger resistivity of Ta as compared to other layers. Also shown in the inset is the FeMn thickness dependence of H_I. The net effective field is obtained as $H_{\rm FL} = H_I - H_{\rm Oe} - H_{\rm FL}({\rm Ta})$. As shown in Fig. 12(d), all the samples exhibit a nonzero $H_{\rm FL}$ except for the $t_{\rm FeMn} = 4$ nm sample in which H_I and $H_{\rm Oe}$ are comparable. As shown clearly in the inset of Fig. 12(d), the contribution of Ta layer to the effective field is negligible.

After excluding the contribution from Ta as main source, the net $H_{\rm FL}$ must be induced by the spin current from the Pt layer since the spin Hall angle of FeMn is very small [31,32]. Considering the fact that the Pt layer has a same thickness in all the samples, it is plausible to assume that the spin Hall angle and thickness scaling factor $[1 - 1/\cosh(d/\lambda_{\rm HM})]$ of Pt are the same among the different samples. We further assume that the moment per unit area of NiFe($M_s t_{\rm NiFe}$) is also a constant. Therefore, the decrease in effective field in the NiFe layer can only come from two sources: (1) relaxation of spin current in FeMn and (2) reduced spin-mixing conductance ($G_{\rm mix}$) at the FeMn/Pt and NiFe/FeMn interfaces as compared to the single NiFe/Pt interface. Earlier reports [32,33] found that spin transport in FM/normal metal (NM)/FeMn structures is mainly dependent on the FM/NM interface and the spin relaxation inside FeMn. Therefore, rather than a dramatic modification of $G_{\rm mix}$ at the interfaces with the presence of the FeMn layer, the absorption of spin current by FeMn is more likely the major cause for decreased spin current entering NiFe. This spin-absorption explanation is also consistent with the large $H_{\rm FL}$ observed in FeMn/Pt bilayers.

The spin current in the NiFe layer induced by Pt in the NiFe/FeMn/Pt trilayer can be modeled using the drift-diffusion approach. Due to the relatively large size of the Hall bar sample in the xy plane, the spin current can be treated as nonequilibrium spins flowing in the z direction with polarization in the y direction. Therefore, the spatial distribution of spin current in NiFe/FeMn can be written as [54]

$$j_i(z) = -\frac{1}{2e\rho_i}\frac{\partial \Delta\mu_i(z)}{\partial z}, \tag{6}$$

where $i = 1$ refers to FeMn, $i = 2$ denotes NiFe, $\Delta\mu_i$ and j_i are the net spin accumulation and spin-current density in layer i, respectively, and ρ_i is resistivity of layer i. The spin accumulation satisfies the following diffusion equation [62]:

$$\frac{\partial^2 \Delta\mu_i(z)}{\partial z^2} = \frac{\Delta\mu_i(z)}{{\lambda_i}^2}, \tag{7}$$

where λ_i is the spin diffusion length of layer i. The general solution for $\Delta\mu_i$ is $\Delta\mu_i(z) = A_i \exp(z/\lambda_i) + B_i \exp(-z/\lambda_i)$. To obtain specific solutions, we need to set up proper boundary conditions. As discussed above, the effect of Ta layer is negligible. In order to obtain a simple analytical solution, we assume that the spin current is zero at the NiFe/Ta

interface. Based on this assumption, we adopted the following boundary conditions: $j_1(0) = j_0$, $j_2(t_2) = 0$, $j_1(t_1) = j_2(t_1)$, and $\Delta\mu_1(t_1) = \Delta\mu_2(t_1)$, where t_1 is the thicknesses of the FeMn (t_{FeMn}), t_2 is the sum of the thickness of FeMn and NiFe layer ($t_{\mathrm{FeMn}} + t_{\mathrm{NiFe}}$), and j_0 is the spin current generated by Pt entering FeMn. Substituting the boundary conditions into Eqs. (6) and (7), the spin-current density at the interface entering NiFe can be derived as

$$j(t_1)/j_0 = \frac{2\lambda_1\rho_1 A(1-B^2)}{\lambda_1\rho_1(1+A^2)(1-B^2)+\lambda_2\rho_2(1-A^2)(1+B^2)}, \tag{8}$$

where $A = \exp(t_{\mathrm{FeMn}}/\lambda_1), B = \exp(t_{\mathrm{NiFe}}/\lambda_2)$. Comparing it with Eq. (1), we can see that the spin absorption in the FeMn layer gives an additional scaling factor for spin current to be delivered to the NiFe layer. In the extreme case when t_{NiFe} approaches infinite, i.e., $B \to \infty$, Eq. (8) is reduced to $j(t_1)/j_0 \approx 1/A$, if $\lambda_1\rho_1 \approx \lambda_2\rho_2$, which is the exponential decay formula used in Refs. [27,30,33] to obtain the spin diffusion length in AFMs. On the other hand, if $t_1 = 0$, $j(t_1)/j_0 = 1$, which means that the spin current generated by Pt will enter NiFe directly without absorption in the FeMn layer. In our sample, since the NiFe thickness is comparable to that of FeMn, the effect of NiFe can no longer be ignored. Note that the difference in G_{mix} of NiFe/Pt and FeMn/Pt interfaces is ignored for simplicity, and we also assume that G_{mix} is independent of FeMn thicknesses. Although from the results in Fig. 9(b) it may be inferred that G_{mix} is thickness dependent (i.e. j_0 is dependent on t_{FeMn}), in the above derivation, we mainly focus on the spin-current decay in FeMn and consider j_0 as a constant. By scaling the H_{FL} obtained in the NiFe layer using the resistivity of the films obtained above and the spin-diffusion length of NiFe ($\lambda_2 = 3$ nm) [63], as shown in Fig. 12(d), the spin-diffusion length of FeMn(λ_1) is obtained as 2 nm. This value is comparable to earlier reports of 1.9 nm (Ref. [33]) and 1.8 ± 0.5 nm (Ref. [32]). The short spin-diffusion length is consistent with the previous understanding of AFM as a good "spin sink" [64,65]. The effective absorption of spin current by FeMn is consistent with the large SOT effect observed in FeMn/Pt bilayers. Although the spin configuration of FeMn in the bilayer sample may be different from that of the trilayer sample due to the insertion of the NiFe seed layer in the latter, we foresee that the difference, if any, is only qualitative; it will not affect the results and conclusion drawn in this section in a fundamental way.

The difference in FeMn thickness dependence of H_{FL} between the bilayer [Fig. 8(b)] and trilayer [Fig. 12(d)] cases can be understood as follows. As we discussed in Sec. III C [see Fig. 9(b)], although the spin current traveling across FeMn/Pt deceases almost linearly with t_{FeMn}, the H_{FL} in FeMn/Pt bilayer is mainly determined by the thickness dependence of the magnetic moment in FeMn ($M_{\mathrm{FeMn}}\ t_{\mathrm{FeMn}}$) [see Fig. 8(c)]. On the other hand, for the NiFe/FeMn/Pt trilayer case, H_{FL} is for the NiFe layer (the signal from FeMn is masked out by that of NiFe due to its much smaller magnetization), and thus it is a measure of spin current that travels across the FeMn layer and eventually enters the NiFe layer. As can be seen from Eq. (8), the spin current traveling in FeMn further decays by a factor of $\frac{2\lambda_1\rho_1 A(1-B^2)}{\lambda_1\rho_1(1+A^2)(1-B^2)+\lambda_2\rho_2(1-A^2)(1+B^2)}$ upon reaching the NiFe/FeMn interface. This decay, together with the almost linear decay of SMR [see Fig. 8(b)], gives the overall decay of spin current upon reaching the NiFe/FeMn interface. This spin current is further converted to H_{FL} in NiFe through the magnetic moment ($M_{\mathrm{NiFe}}t_{\mathrm{NiFe}}$). Since the NiFe thickness is fixed among the samples, the FeMn thickness dependence of H_{FL} in NiFe of the trilayers should be the same as that of the spin current reaching the NiFe/FeMn interface. This explains why the H_{FL} in NiFe decreases monotonically with the FeMn thickness, which is different from that in FeMn.

Before we conclude, it is worth pointing out that the FeMn investigated in this paper has a polycrystalline structure, and due to the ultrathin thickness, the AFM order may not be well defined as in the bulk material. We foresee this as the main challenge in investigating and exploiting SOT effect in AFM materials, i.e., SOT is more prominent in ultrathin layers, but most AFM requires a finite thickness to develop a stable AFM order at RT. To overcome this difficulty, it is necessary to develop AFM materials which allow effective generation of nonequilibrium spins in the bulk. One of the possible candidates is an AFM with BIA and strong SO interaction [48].

IV. CONCLUSIONS

In summary, our systematic studies revealed that spin Hall current from Pt induces SOT in the FeMn layer in FeMn/Pt bilayers, which is able to induce canting of the spin sublattices of FeMn when its thickness is below 5 nm. Based on current-dependent PHE measurements, a large fieldlike effective field of 2.05×10^{-5} to 2.44×10^{-5} Oe ($\mathrm{A}^{-1}\ \mathrm{cm}^2$) was obtained for FeMn in the thickness range of 2–5 nm, which is attributed to the small net moment in FeMn as compared to its FM counterpart. The origin of the moment was further investigated by the magnetometry measurements, and is found to be mainly from FeMn itself arising from the canting of the uncompensated spin sublattices. The spin-canting process can be explained reasonably well based on the macrospin model by taking into account the current-generated effective field. Further investigations on NiFe/FeMn/Pt trilayers show that spin current from Pt is strongly absorbed by the FeMn layer with a spin-diffusion length of around 2 nm, which explains why the SOT effect is strong in FeMn/Pt bilayers when t_{FeMn} is small and becomes negligible when $t_{\mathrm{FeMn}} > 10$ nm. Although it remains a challenge to ensure the presence of both well-defined AFM order and large SOT in thin AFM layers, the results presented here shall stimulate further studies on spin transport in AFM materials with different types of crystalline and spin structures.

ACKNOWLEDGMENTS

The authors wish to thank Prof. Jingshen Chen, Dr. Kaifeng Dong, and Dr. Baoyu Zong from National University of Singapore, and Dr. Wendong Song of Data Storage Institute for their assistance in magnetic measurements. Y.H.W. would like to acknowledge support from the Singapore National Research Foundation, Prime Minister's Office, under its Competitive Research Programme (Grant No. NRF-CRP10-2012-03) and Ministry of Education, Singapore under its Tier 2 Grant (Grant No. MOE2013-T2-2-096). M.S.M. and K.Y. acknowledge the

support of IMRE, A*STAR under Project No. IMRE/10-1C0107. R.-W.L. acknowledges the support of the National Natural Foundation of China (Grants No. 11274321 and No. 51525103) and the Ningbo International Cooperation Projects (Grant No. 2014D10005). S.Z. is partially supported by the U.S. National Science Foundation (Grant No. ECCS-1404542). Y.H.W. is a member of the Singapore Spintronics Consortium (SG-SPIN).

[1] A. Chernyshov, M. Overby, X. Liu, J. K. Furdyna, Y. Lyanda-Geller, and L. P. Rokhinson, Nat. Phys. **5**, 656 (2009).
[2] I. M. Miron, G. Gaudin, S. Auffret, B. Rodmacq, A. Schuhl, S. Pizzini, J. Vogel, and P. Gambardella, Nat. Mater. **9**, 230 (2010).
[3] I. M. Miron, K. Garello, G. Gaudin, P. J. Zermatten, M. V. Costache, S. Auffret, S. Bandiera, B. Rodmacq, A. Schuhl, and P. Gambardella, Nature **476**, 189 (2011).
[4] L. Liu, O. J. Lee, T. J. Gudmundsen, D. C. Ralph, and R. A. Buhrman, Phys. Rev. Lett. **109**, 096602 (2012).
[5] L. Liu, C. F. Pai, Y. Li, H. W. Tseng, D. C. Ralph, and R. A. Buhrman, Science **336**, 555 (2012).
[6] A. Manchon and S. Zhang, Phys. Rev. B **78**, 212405 (2008).
[7] K. Garello, I. M. Miron, C. O. Avci, F. Freimuth, Y. Mokrousov, S. Blugel, S. Auffret, O. Boulle, G. Gaudin, and P. Gambardella, Nat. Nanotechnol. **8**, 587 (2013).
[8] C. O. Avci, K. Garello, C. Nistor, S. Godey, B. Ballesteros, A. Mugarza, A. Barla, M. Valvidares, E. Pellegrin, A. Ghosh, I. M. Miron, O. Boulle, S. Auffret, G. Gaudin, and P. Gambardella, Phys. Rev. B **89**, 214419 (2014).
[9] G. Yu, P. Upadhyaya, Y. Fan, J. G. Alzate, W. Jiang, K. L. Wong, S. Takei, S. A. Bender, L.-T. Chang, Y. Jiang, M. Lang, J. Tang, Y. Wang, Y. Tserkovnyak, P. K. Amiri, and K. L. Wang, Nat. Nanotechnol. **9**, 548 (2014).
[10] X. Fan, H. Celik, J. Wu, C. Ni, K. J. Lee, V. O. Lorenz, and J. Q. Xiao, Nature Commun. **5**, 3042 (2014).
[11] K. Masashi, S. Kazutoshi, F. Shunsuke, M. Fumihiro, O. Hideo, M. Takahiro, C. Daichi, and O. Teruo, Appl. Phys. Express **6**, 113002 (2013).
[12] X. Fan, J. Wu, Y. Chen, M. J. Jerry, H. Zhang, and J. Q. Xiao, Nature Commun. **4**, 1799 (2013).
[13] M. Jamali, K. Narayanapillai, X. Qiu, L. M. Loong, A. Manchon, and H. Yang, Phys. Rev. Lett. **111**, 246602 (2013).
[14] T. Nan, S. Emori, C. T. Boone, X. Wang, T. M. Oxholm, J. G. Jones, B. M. Howe, G. J. Brown, and N. X. Sun, Phys. Rev. B **91**, 214416 (2015).
[15] C.-F. Pai, Y. Ou, L. H. Vilela-Leão, D. C. Ralph, and R. A. Buhrman, Phys. Rev. B **92**, 064426 (2015).
[16] A. H. MacDonald and M. Tsoi, Phil. Trans. R. Soc. **369**, 3098 (2011).
[17] E. V. Gomonay and V. M. Loktev, Low Temp. Phys. **40**, 17 (2014).
[18] A. S. Núñez, R. A. Duine, P. M. Haney, and A. H. MacDonald, Phys. Rev. B **73**, 214426 (2006).
[19] R. A. Duine, P. M. Haney, A. S. Núñez, and A. H. MacDonald, Phys. Rev. B **75**, 014433 (2007).
[20] P. M. Haney, D. Waldron, R. A. Duine, A. S. Núñez, H. Guo, and A. H. MacDonald, Phys. Rev. B **75**, 174428 (2007).
[21] Y. Xu, S. Wang, and K. Xia, Phys. Rev. Lett. **100**, 226602 (2008).
[22] S. Urazhdin and N. Anthony, Phys. Rev. Lett. **99**, 046602 (2007).
[23] X.-L. Tang, H.-W. Zhang, H. Su, Z.-Y. Zhong, and Y.-L. Jing, Appl. Phys. Lett. **91**, 122504 (2007).
[24] N. V. Dai, N. C. Thuan, L. V. Hong, N. X. Phuc, Y. P. Lee, S. A. Wolf, and D. N. H. Nam, Phys. Rev. B **77**, 132406 (2008).
[25] Z. Wei, A. Sharma, A. S. Nunez, P. M. Haney, R. A. Duine, J. Bass, A. H. MacDonald, and M. Tsoi, Phys. Rev. Lett. **98**, 116603 (2007).
[26] C. Hahn, G. de Loubens, V. V. Naletov, J. Ben Youssef, O. Klein, and M. Viret, Europhys. Lett. **108**, 57005 (2014).
[27] H. Wang, C. Du, P. C. Hammel, and F. Yang, Phys. Rev. B **91**, 220410(R) (2015).
[28] T. Moriyama, M. Nagata, K. Tanaka, K-J. Kim, H. Almasi, W. G. Wang, and T. Ono, arXiv:1411.4100.
[29] T. Moriyama, S. Takei, M. Nagata, Y. Yoshimura, N. Matsuzaki, T. Terashima, Y. Tserkovnyak, and T. Ono, Appl. Phys. Lett. **106**, 162406 (2015).
[30] H. Wang, C. Du, P. C. Hammel, and F. Yang, Phys. Rev. Lett. **113**, 097202 (2014).
[31] C. Du, H. Wang, F. Yang, and P. C. Hammel, Phys. Rev. B **90**, 140407(R) (2014).
[32] W. Zhang, M. B. Jungfleisch, W. Jiang, J. E. Pearson, A. Hoffmann, F. Freimuth, and Y. Mokrousov, Phys. Rev. Lett. **113**, 196602 (2014).
[33] P. Merodio, A. Ghosh, C. Lemonias, E. Gautier, U. Ebels, M. Chshiev, H. Béa, V. Baltz, and W. E. Bailey, Appl. Phys. Lett. **104**, 032406 (2014).
[34] J. Liu, T. Ohkubo, S. Mitani, K. Hono, and M. Hayashi, Appl. Phys. Lett. **107**, 232408 (2015).
[35] S. Cho, S. H. Baek, K. D. Lee, Y. Jo, and B. G. Park, Sci. Rep. **5**, 14668 (2015).
[36] H. Nakayama, M. Althammer, Y.-T. Chen, K. Uchida, Y. Kajiwara, D. Kikuchi, T. Ohtani, S. Geprägs, M. Opel, S. Takahashi, R. Gross, G. E. W. Bauer, S. T. B. Goennenwein, and E. Saitoh, Phys. Rev. Lett. **110**, 206601 (2013).
[37] S. Y. Huang, X. Fan, D. Qu, Y. P. Chen, W. G. Wang, J. Wu, T. Y. Chen, J. Q. Xiao, and C. L. Chien, Phys. Rev. Lett. **109**, 107204 (2012).
[38] Y. M. Lu, Y. Choi, C. M. Ortega, X. M. Cheng, J. W. Cai, S. Y. Huang, L. Sun, and C. L. Chien, Phys. Rev. Lett. **110**, 147207 (2013).
[39] D. Qu, S. Y. Huang, J. Hu, R. Wu, and C. L. Chien, Phys. Rev. Lett. **110**, 067206 (2013).
[40] M. Kowalewski, W. H. Butler, N. Moghadam, G. M. Stocks, T. C. Schulthess, K. J. Song, J. R. Thompson, A. S. Arrott, T. Zhu, J. Drewes, R. R. Katti, M. T. McClure, and O. Escorcia, J. Appl. Phys. **87**, 5732 (2000).
[41] Y. Liu, C. Jin, Y. Q. Fu, J. Teng, M. H. Li, Z. Y. Liu, and G. H. Yu, J. Phys. D: Appl. Phys. **41**, 205006 (2008).
[42] Y. Liu, Y. Q. Fu, S. Liu, C. Jin, M. H. Li, and G. H. Yu, J. Appl. Phys. **107**, 023912 (2010).
[43] R. Jungblut, R. Coehoorn, M. T. Johnson, J. aan de Stegge, and A. Reinders, J. Appl. Phys. **75**, 6659 (1994).

[44] X. Y. Lang, W. T. Zheng, and Q. Jiang, Nanotechnology **18**, 155701 (2007).
[45] J. Kim, J. Sinha, S. Mitani, M. Hayashi, S. Takahashi, S. Maekawa, M. Yamanouchi, and H. Ohno, Phys. Rev. B **89**, 174424 (2014).
[46] Y.-T. Chen, S. Takahashi, H. Nakayama, M. Althammer, S. T. B. Goennenwein, E. Saitoh, and G. E. W. Bauer, Phys. Rev. B **87**, 144411 (2013).
[47] J. Kim, J. Sinha, M. Hayashi, M. Yamanouchi, S. Fukami, T. Suzuki, S. Mitani, and H. Ohno, Nat. Mater. **12**, 240 (2013).
[48] J. Železný, H. Gao, K. Výborný, J. Zemen, J. Mašek, A. Manchon, J. Wunderlich, J. Sinova, and T. Jungwirth, Phys. Rev. Lett. **113**, 157201 (2014).
[49] H. B. M. Saidaoui, A. Manchon, and X. Waintal, Phys. Rev. B **89**, 174430 (2014).
[50] Y. M. Lu, J. W. Cai, S. Y. Huang, D. Qu, B. F. Miao, and C. L. Chien, Phys. Rev. B **87**, 220409(R) (2013).
[51] M. Ekholm and I. A. Abrikosov, Phys. Rev. B **84**, 104423 (2011).
[52] P. Bisantit, G. Mazzonet, and F. Sacchettig, J. Phys. F: Met. Phys. **17**, 1425 (1987).
[53] K. Nakamura, T. Ito, A. J. Freeman, L. Zhong, and J. Fernandez-de-Castro, Phys. Rev. B **67**, 014405 (2003).
[54] D. Spisak and J. Hafner, Phys. Rev. B **61**, 11569 (2000).
[55] W. J. Antel, Jr. F. Perjeru, and G. R. Harp, Phys. Rev. Lett. **83**, 1439 (1999).
[56] F. Y. Yang and C. L. Chien, Phys. Rev. Lett. **85**, 2597 (2000).
[57] V. S. Gornakov, Y. P. Kabanov, O. A. Tikhomirov, V. I. Nikitenko, S. V. Urazhdin, F. Y. Yang, C. L. Chien, A. J. Shapiro, and R. D. Shull, Phys. Rev. B **73**, 184428 (2006).
[58] A. G. Gurevich and G. A. Melkov, *Magnetization Oscillations and Waves* (CRC Press, Boca Raton, 1996), p. 59.
[59] G. Vallejo-Fernandez, L. E. Fernandez-Outon, and K. O'Grady, J. Phys. D: Appl. Phys. **41**, 112001 (2008).
[60] M. R. Fitzsimmons, J. A. Eastman, R. B. Von Dreele, and L. J. Thompson, Phys. Rev. B **50**, 5600 (1994).
[61] M. J. Donahue and D. G. Porter, *OOMMF User's Guide Version 1.2a5*, http://math.nist.gov/oommf.
[62] A. Fert and H. Jaffrès, Phys. Rev. B **64**, 184420 (2001).
[63] J. Bass and W. P. Pratt, J. Phys.: Condens. Matter **19**, 183201 (2007).
[64] R. Acharyya, H. Y. T. Nguyen, W. P. Pratt, and J. Bass, J. Appl. Phys. **109**, 07C503 (2011).
[65] H. Ulrichs, V. E. Demidov, S. O. Demokritov, W. L. Lim, J. Melander, N. Ebrahim-Zadeh, and S. Urazhdin, Appl. Phys. Lett. **102**, 132402 (2013).